remote sensing

MDPI

Article

Investigation and Analysis of All-Day Atmospheric Water Vapor Content over Xi'an Using Raman Lidar and Sunphotometer Measurements

Yufeng Wang, Liu Tang, Tianle Gao, Qing Wang, Chuan Lu, Yuehui Song and Dengxin Hua *

School of Mechanical and Precision Instrument Engineering, Xi'an University of Technology, Xi'an 710048, China; wyfecnu@126.com (Y.W.); tangliu37@163.com (L.T.); nardus88@163.com (T.G.); wangqing@xaut.edu.cn (Q.W.); eerefgt1997@163.com (C.L.); songyuehui@xaut.edu.cn (Y.S.)

* Correspondence: dengxinhua@xaut.edu.cn

Received: 14 May 2018; Accepted: 13 June 2018; Published: 14 June 2018

Abstract: All-day atmospheric water vapor content measurements determined by Raman lidar and a sunphotometer were combined to investigate the all-day variation characteristics in the water vapor distribution in Xi'an, China (34.233°N, 108.911°E). To enhance the daytime lidar performance, the wavelet threshold de-noising method is used to filter out the strong solar background light, and effective denoised results are demonstrated with the following optimization: wavelet sym6, the improved threshold function, and the improved threshold selection. The denoised system signal-to-noise ratio (SNR) for the water vapor daytime measurement is validated, with an enhancement of ~3.4 times up to a height of 3 km compared to that of the original signal. The time series of the atmospheric water vapor mixing ratio profiles and the obtained precipitable water vapor (PWV) measured by Raman lidar are used to reveal the temporal and spatial variations in water vapor, and the comparisons with the total column water vapor content (TCWV) measured by a sunphotometer validate the daytime variation trend of the water vapor. All-day continuous observations clearly present a consistent variation trend in the water vapor between the sunphotometer and Raman lidar measurements. The correlation analysis between TCWV and PWV at the layers below 850 hPa and below 700 hPa yields a good positive correlation coefficient (>0.75), indicating that PWV determination in the bottom layer by Raman lidar can directly reflect the variations in the total water vapor content. Moreover, different diurnal variation trends in water vapor are also observed, that is, a downward trend from the afternoon to the night, or a tendency of being high in the morning and afternoon and low at noon, demonstrating the high temporal-spatial variation characteristics of water vapor and close correlation with weather changes. The results reflected and validated that the diurnal variation in water vapor is complicated and can be an indicator of the weather to a certain extent.

Keywords: water vapor; Raman lidar; sunphotometer; all-day

1. Introduction

Atmospheric water vapor plays an important role in hydrological processes, atmospheric circulation, and weather systems [1,2]. Water vapor is the primary greenhouse gas whose radiative effects may amplify the response to changes in climate, leading to further global warming. In addition, water vapor is closely related to surface evaporation, cloud formation, precipitation, and circulation transportation [3–5]. Precipitable water vapor (PWV) is defined as a vertically integrated water vapor column within a layer; it is the most active component in the global hydrological cycle, which in turn makes water vapor an important factor influencing regional climate change, water balance, and energy

balance [6,7]. Research on the temporal and spatial distribution of atmospheric water vapor and PWV not only helps to study global and regional climate change, cloud formation, and precipitation processes, but also provides a theoretical basis for atmospheric water resources.

Lidar is a powerful tool used in remote sensing for characterizing atmospheric components and atmospheric properties [8–11]. With the development of laser technology and Raman spectroscopy, Raman lidar has succeeded in measuring atmospheric temperature, water vapor, and aerosols [12–14]. Vibrational Raman scattering signals from water vapor molecules (H_2O) and nitrogen molecules (N_2) have been widely used in the detection of water vapor profiles [15,16]. The potential of Raman lidars is not only to investigate synchronous multi-parameters profiles and the correlations among them, but also to study aerosol hygroscopic growth by combining water vapor and aerosols [17–20]. Many ground-based Raman lidar systems currently exist around the world, and significant achievements have been made in the measurement of water vapor and aerosol profiles [21–24]. At present, atmospheric water vapor mixing ratio profiles can be achieved up to the entire troposphere by Raman lidars. However, methods for all-day water vapor measurements with high precision must still be developed because of the strong solar background light in the daytime.

The sunphotometer, which is an important tool for atmospheric research and meteorological observation, has advantages for studying the optical and physical properties of aerosol particles in the daytime [25,26]. Aerosol size distribution, total precipitable water, and optical thickness can be obtained by direct radiation analysis of the solar forcing. Oleg Dubovik et al. measured four types of aerosols and studied the average optical characteristics in different regions using a sunphotometer [27]. Hu Xiuqing et al. measured the total precipitable water using CE-318 to determine the input parameters of the radiation transmission model [28]. Many detailed studies have also been conducted in terms of calibration methods, retrieval algorithms, and so on [29,30].

Considering the complementarity of sunphotometer and lidar techniques, in this paper, the combination of a Raman lidar and sunphotometer is applied to investigate the all-day variation characteristics in the water vapor distribution in Xi'an. To extract the weak Raman scattering signals of water vapor from strong solar background light, the wavelet threshold de-noising method is used, as presented in detail in Section 3; using this technique, the daytime performance of Raman lidar is first validated. In Section 4, water vapor profiles and PWV characterized by Raman lidar and the total column water vapor content (TCWV) characterized by the sunphotometer are combined to study the temporal and spatial variations in water vapor in the daytime. The results from the two continuous observations clearly reveal the all-day variation trend, and the correlation between them is also analyzed.

2. Configuration and Retrieval Method

2.1. Raman Lidar and Retrieval Methods for Water Vapor

The ultraviolet Raman lidar system used in this study was developed at Xi'an University of Technology. A schematic diagram of the system is presented in Figure 1. The system employs a pulsed Nd:YAG laser as a light source. The laser operates at a frequency-tripled wavelength of 354.7 nm and has a 20 Hz repetition rate, an energy output of 150 mJ, and a 9 ns full width at half maximum (FWHM) pulse duration. Returned signals are collected using a 600 mm Newtonian telescope and are then coupled with a multimode optical fiber and guided into a spectroscopic box. A set of dichroic mirrors (DMs) and narrow-band interference filters (IFs) is used to construct a high-efficiency polychromator, which divides the returned signals into three channels: channel 1 is used for the detection of elastic Mie-Rayleigh signals, and channels 2 and 3 are used to detect the vibrational Raman signals of nitrogen and water vapor molecules at central-wavelengths of 386.7 nm and 407.6 nm, respectively. Taking into account the influence of strong solar background light, a receiving optical fiber with a diameter of 200 μm and an interference filter with a bandwidth of 0.5 nm are used.

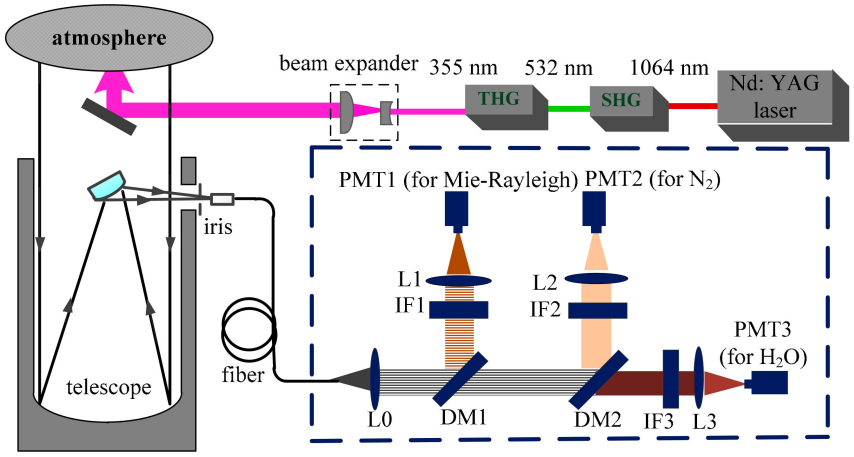

Figure 1. Schematic of the Raman lidar system for water vapor measurement. (SHG: Second-harmonic generation, THG: Third-harmonic generation, DM: Dichroic mirror, IF: Interference filter).

According to its definition, the atmospheric water vapor mixing ratio $w(z)$ is defined as the mass water vapor divided by the mass of dry air in a given volume, which is given as [15]:

$$w(z) = \frac{N_H(z)M_H}{N_{dry}(z)M_{dry}} \tag{1}$$

where $N_H(z)$ and N_{dry} are the density of the water vapor and dry air, respectively; and M_H and M_{dry} are the molecular weight of the water vapor (~18 g/mol) and dry air (an averaged quantity whose value is 28.94 g/mol), respectively. Considering that N_2 molecular forms a constant fraction (~0.78) of dry air in the lower atmosphere, it is apparent that the water vapor mixing ratio can be calculated using the ratio of the Raman water vapor (λ_H = 407.5 nm) and Nitrogen signals (λ_N = 386.7 nm), expressed as [15]:

$$w(z) = 0.485 \times \frac{N_H(z)}{N_N(z)} = 0.485 \times \frac{P_H(z)}{P_N(z)} \cdot \frac{k_N}{k_H} \cdot \frac{\sigma_N(\pi)}{\sigma_H(\pi)} \cdot \exp\left\{ \int_0^z [\alpha_{\lambda_H}(z') - \alpha_{\lambda_N}(z')]dz' \right\} \tag{2}$$

where the subscripts H and N denote H_2O and N_2 molecules, respectively; P is the output power of the channel; σ is the cross section of Raman scattering; α_λ is the extinction coefficient at the wavelength λ; and k is the system efficiency factor, including the optical efficiency and electrical efficiency of system. Moreover, k_N/k_H is the system constant, which can be calibrated by comparison with radiosonde data at the same height. For our lidar, the system calibration was performed with the radiosonde data obtained from the local Meteorological Bureau of Xi'an (~8 km from the lidar) at 20:00 CST, and a fixed height of ~1000 m is used as the calibration height.

The mixing ratio $q(z)$ is defined as the ratio of the mass of water vapor to the total mass of wet air, and it is related to the water vapor mixing ratio $w(z)$ and given as:

$$q(z) = \frac{w(z)}{w(z)+1} \tag{3}$$

The precipitable water vapor (PWV) is defined as the vertically integrated water vapor column (unit: mm) within a layer and can be calculated as:

$$\mathrm{PWV} = \frac{1}{g\rho}\int_{p_0}^{p} q\,dp = \frac{1}{g\rho}\sum_{i=1}^{n} \bar{q}\Delta p \tag{4}$$

where p_0 and p are atmospheric pressures (unit: Pascal) at the layer's upper and lower boundaries, respectively; ρ is the vapor density; and g is the acceleration of gravity (9.806 ms^{-2}). Thus, the water vapor mixing ratio profiles and PWV in different layers can be obtained by the Raman lidar.

2.2. Sunphotometer and Retrieval Methods for Total Column Water Vapor Content

The sunphotometer used in this paper is PREDE POM-02 from Japan, and it is provided with 11 channels: 315 nm, 340 nm, 380 nm, 400 nm, 500 nm, 675 nm, 870 nm, 940 nm, 1020 nm, 1627 nm, and 2200 nm. The non-absorbed band in visible spectra is normally used for retrieving the optical and physical properties of aerosol particles, and the strong water vapor absorption 940 nm band has been used to determine water column abundance in the atmosphere when the path to the sun is clear of clouds [31].

At 340, 380, 400, 500, and 870 nm wavelengths with weak absorption by atmospheric gases, the total optical depth of τ_λ is derived based on the Beer-Lambert-Bouguer law, as follows [32]:

$$V_\lambda = V_{0\lambda} R^{-2} \exp[-m\tau_\lambda] \tag{5}$$

where, for each channel (wavelength), the subscript λ denotes the wavelength; V_λ is the signal measured by the sunphotometer at wavelength λ; $V_{0\lambda}$ represents the calibration coefficients at wavelength λ, and can be obtained by the Langley calibration method; R is the Earth-Sun distance in Astronomical units at the time of observation; m is the optical air mass; and τ_λ is the total optical depth at wavelength λ. Taking the natural logarithms of both sides of Equation (5), the total optical depth τ_λ is given as:

$$\tau_\lambda = -\frac{1}{m} \ln \frac{V_\lambda R^2}{V_{0\lambda}} \tag{6}$$

The Rayleigh optical depth $\tau_{m\lambda}$ at different wavelengths λ can be obtained from atmospheric models, and is given as:

$$\tau_{m\lambda} = \frac{p}{p_0} 0.0088 \lambda^{-4.05} \tag{7}$$

where p_0 is the standard atmospheric pressure and p is the practical atmospheric pressure.

In the case of neglecting the ozone absorption, therefore, aerosol optical depth (AOD or $\tau_{a\lambda}$) at wavelength λ is obtained by:

$$\tau_{a\lambda} = \tau_\lambda - \tau_{m\lambda} \tag{8}$$

AOD at different wavelengths follows the Junge distribution, as follows:

$$\tau_a(\lambda) = \beta \lambda^{-\alpha} \tag{9}$$

where α and β are the Ångström exponent and turbidity coefficient, respectively, and can be derived using the linear fitting of the AODs of 340, 380, 400, 500, and 870 nm channels. Thus, the aerosol optical depth at 940 nm (τ_{a940}) can be obtained.

It is pertinent to mention that the 940 nm wavelength is greatly affected by water vapor absorption. As such, the most significant parameter used to derive water vapor in the instrument is the signal data from the 940 nm channel. Because of the nonlinear contribution from water vapor in the 940 nm channel, the response of this channel by the sunphotometer is given as [29,31,32]:

$$V_w = V_{0w} R^{-2} \exp(-m\tau_{a940}) T_W \tag{10}$$

where the subscript w represents the water vapor channel and Tw is the water vapor transmission rate, which is given as:

$$T_W = \exp\left(-a\omega^b\right) \tag{11}$$

where a and b are instrument constants numerically derived for the 940 nm filter, and here a = 0.585 and b = 0.573; ω is the titled atmospheric water vapor and can be written as $\omega = \mathrm{m}p_{\mathrm{W}}$; and p_{W} is the total column water vapor. Thus, the total column water vapor 940 nm band is selected for retrieving the total column water vapor (TCWV), which can be written as:

$$p_{\mathrm{W}} = \left(-\frac{\ln\left(\mathrm{VR}^2/\mathrm{V}_0 + \mathrm{m}\tau\right)}{\mathrm{am}^{\mathrm{b}}} \right)^{1/\mathrm{b}} \tag{12}$$

3. Daytime Performance of Raman Lidar

In a view of all-day lidar detection, lidar return signals in the daytime are likely to be contaminated or even drowned out by noise; thus, the detection performance of lidar is greatly reduced. Compared with the elastic Mie-Rayleigh scattering signals, Raman scattering signals of atmospheric molecules should be smaller by three to four orders of magnitude. Therefore, determining how to extract weak Raman scattering signals from strong background light is one of the key difficulties in the daytime Raman lidar measurements. The wavelet threshold de-noising method has been widely used in signal analysis, image processing, fault diagnosis, and other fields. Using wavelet decomposition and wavelet reconstruction, the noise can be effectively removed from real signals [33–36]. In this section, the wavelet threshold de-noising method is used to extract the Raman scattering signal of water vapor from the background light, and the detailed de-noising process is discussed and validated regarding its improvement in daytime Raman lidar for water vapor measurements.

3.1. Wavelet De-Noising Method

The lidar return signal with noise can be given as:

$$f(t) = s(t) + \sigma e(t), \qquad 1 \le t \le N \tag{13}$$

where $s(t)$ represents the true value of the lidar return signal, $e(t)$ is the white noise caused by the electronic noise and stray light, σ is the noise coefficient, and N is the length of the discrete sampling sequence $f(t)$. Regarding the daytime lidar measurement, background light from the sun and the electrical noise by the detection system constitute the main noise.

The purpose of wavelet de-noising is to reduce the degree of contamination of $s(t)$ by $e(t)$. Discrete signals by wavelet transform or decomposition at different resolutions show different characteristics, so the noise can be reduced using different threshold and wavelet coefficients. Therefore, $f(t)$ is a finite power function, and then $f(t) \in L^2(R)$ (square-integral real number vector space). According to the definition of wavelets multi-resolution analysis, in the given vector space Vj, $f(t)$ can also be expressed as a series expansion in terms of the scaling function and wavelets, as follows [36–38]:

$$f(t) = \sum a_k^{j-1} \varphi(2^{j-1}t - k) + \sum d_k^{j-1} \psi(2^{j-1}t - k), \tag{14}$$

where the first summation $\sum a_k^{j-1} \varphi(2^{j-1}t - k)$ represents a function that is in a low-resolution or coarse approximation of $f(t)$, and the second summation $\sum d_k^{j-1} \psi(2^{j-1}t - k)$ is the high-frequency component of $f(t)$, which represents the detailed information of $f(t)$. a_k^{j-1} is the approximation coefficient, and d_k^{j-1} is the wavelet coefficient when the resolution is 2^{j-1}, which are given as [36]:

$$\varphi(2^{j-1}t - l) = \sum h_{k-2l} \varphi(2^j - k), \tag{15}$$

$$\psi(2^{j-1}t - l) = \sum (-1)^k \overline{h_{1-k+2l}} \varphi(2^j - k), \tag{16}$$

$$a_l^{j-1} = \frac{1}{2} \sum \overline{h_{k-2l}} a_k^j, \tag{17}$$

$$d_l^{j-1} = \frac{1}{2}\sum (-1)^k h_{1-k+2l} a_k^j, \tag{18}$$

In Equations (15) and (16), $\varphi(2^{j-1}t - l)$ and $\psi(2^{j-1}t - l)$ represent the scaling function and the wavelet function or mother wavelet, respectively. The subscript j, k, and l belong to the set of integers, and h is the filter function and is determined by the chosen wavelet base. Equations (17) and (18) are recursive equations. So the basic wavelet de-noising principle is to employ wavelet transforms to decompose the return signal according to the multi-scale functions. Because the average power of the wavelet transform coefficients of white noise is inversely proportional to the scale j, the magnitudes of the wavelet transform coefficients of white noise will decay when the order of the wavelet transform increases.

After de-noising, the signal is reconstructed by an inverse wavelet transform and is given as:

$$a_k^j = \sum h_{k-2l} a_l^{j-1} + \sum (-1)^k \overline{h_{1-k+2l}} d_l^{j-1}, \tag{19}$$

Therefore, the basic steps of the wavelet threshold de-noising process are as follows:

(1) First, it is necessary to select the appropriate wavelet base and decomposition level through the de-composition of the original lidar return signals;
(2) Second, it is important to choose the appropriate threshold and threshold function to remove noise and background light from the detected signals;
(3) Finally, it is necessary to reconstruct the signals according to the each level of wavelet decomposition for low-frequency coefficients and high-frequency coefficients.

The effect before and after de-noising can be evaluated by the denoised signal to noise ratio (SNR) and the root mean square error (RMSE), as follows [36]:

$$\mathrm{SNR} = 10 \times \lg \frac{\sum_{i=1}^{n} {s_i}^2}{\sum_{i=1}^{n} (s_i - d_i)^2}, \tag{20}$$

$$\mathrm{RMSE} = \sqrt{\frac{\sum_{i=1}^{n} (s_i - d_i)^2}{n}} \tag{21}$$

where s is the original signal, d is the denoised signal, and n is the signal length.

3.2. De-Noising Processing and Discussion

We conducted wavelet de-noising processing for the measured lidar return signal of water vapor, and the results are discussed in detail in this section. For wavelet de-noising, mother wavelets are wave functions with fast attenuation and a finite length. By stretching and translating, a series of functions can be obtained and defined as the wavelet base functions [38]. These are often used to construct the signals, and also make the signals easy to handle by their inherent characteristics. Generally, there are many kinds of wavelet base functions, including Haar wavelets, Daubechies wavelets, Symlets wavelets, Coiflet wavelets, Molet wavelets, and so on [39–41].

The influence of the wavelet base function on the denoised results is first discussed. Because of the discrete signals, we focused on three common discrete wavelet families: Daubechies (dbs) wavelet base, Symlets (syms) wavelet base, and Coiflet (coifs) wavelet base. Figure 2a shows the denoised SNR and RMSE results by using three wavelet bases with different filter lengths. It can be clearly seen that the denoised SNRs differ greatly under different wavelet bases with filter length. Taking the coifN wavelet base as an example, we can find that the denoised SNR gradually increases from 38.5 to 40 with the filter length increasing from 1 to 5, and the denoised RMSE decreases gradually. Taking symN

and dbN as the wavelet base, the filter length exerts great influence on the denoised results, and the denoised SNR is increased under a shorter filter length, followed by a decline and leveling off under a longer filter length. Overall, the denoised results by symN are better than those by dbN; in particular, the maximum denoised SNR and the minimum RMSE can be achieved with the wavelet bases of sym6 and sym7.

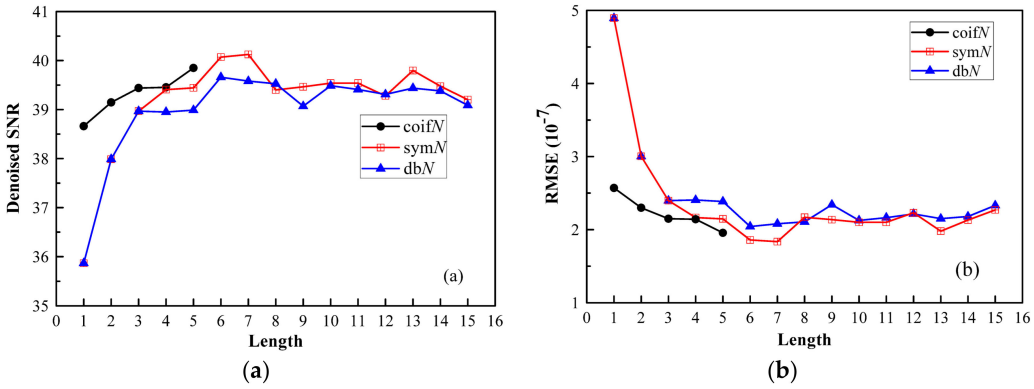

(**a**) (**b**)

Figure 2. Comparison of denoised SNR and RMSE results by wavelet bases with different lengths: (**a**) denoised SNR and (**b**) RMSE.

To express the denoised results more intuitively, we chose several representative wavelet bases with fixed filter lengths to complete the denoising processing. Taking the measurement results obtained at 14:00 CST (Chinese standard time) 12 September 2016, as an example, wavelet de-noising processing was applied, and the denoised range-corrected square signal (RSCS) of water vapor was obtained, as shown in Figure 3. All the heights in this study are relative to the ground level. The curves in the figure were displaced from each other with an offset of $\times 3$. From the original RSCS (black solid line), the effective detection range for daytime water vapor is less than 2000 m because the returned signal above 1500 m is submerged in strong noise. Regarding the red curve, a rough shape with a serration can be observed in the denoised RSCS using the sym2 wavelet base. It is also found that the denoised RSCS values with sym6, sym12, and Db4 are provided with approximately similar shapes, with corresponding denoised SNRs of 40.1, 39.2, and 38.9, respectively, and RMSEs of 1.86×10^{-7}, 2.23×10^{-7}, and 2.41×10^{-7}. By comparison, sym6 is more conducive for obtaining a better denoised effect for water vapor Raman signals in the daytime.

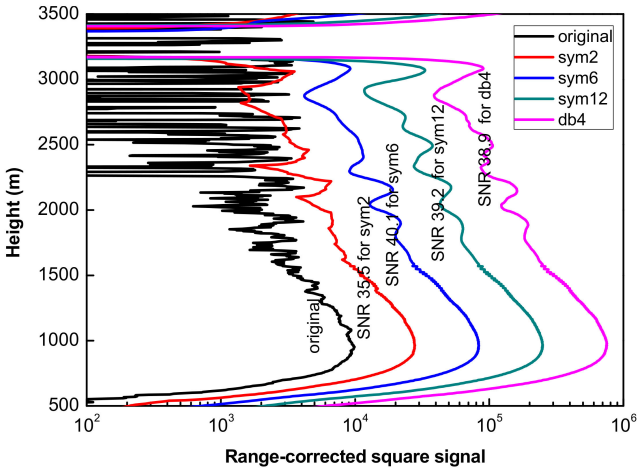

Figure 3. Comparison of the denoised range-corrected square signal of the daytime water vapor Raman scattering signal by wavelet bases of different lengths.

An appropriate threshold selection method directly affects the denoised result because of different thresholds. According to different threshold estimation rules, there are several threshold selection methods, such as the Heuesure threshold (Heuesure), Rigrsure threshold (Rigrsure), Sqtwolog threshold (Sqtwolog), Minimaxi threshold (Minimaxi), and improved threshold [37,42–45]. The Sqtwolog threshold is the most simple and widely applied; however, the wavelet coefficient might be over-killed by its threshold in practical applications. The Rigrsure threshold will result in large noise when the signal to noise ratio is relatively small. The Heuesure threshold is proposed combining the first two threshold selection methods. A fixed threshold is used by the Minimaxi threshold selection method. On the basis of the Sqtwolog threshold, the improved threshold method was developed to obtain different thresholds under different decomposition levels and decomposition scales. Because of different threshold estimation rules, threshold selection methods have their own application scope, so it is particularly important to choose the appropriate threshold during the wavelet de-noising process.

Common threshold selection methods include Heursure, Rigrsure, Sqtwolog, Minimaxi, and improved threshold selection. Here, we discuss the effect of threshold selection methods on the denoised results. As shown in Figure 4, the obtained RSCS and the denoised SNR by using different threshold selection methods are compared with those of the original signals. Regarding the overall shape, it can be seen that a certain denoised effect has been achieved; however, different details exist at certain heights. The denoised RSCS presented obvious oscillation with the Rigrsure threshold method, and a large distortion can be observed at ~2250 m. The distortion phenomenon also exists for other threshold methods except the improved threshold method. A smooth shape and no large distortion were observed in the denoised RSCS using the improved threshold method. The denoised SNRs are also given in the figure, revealing that a denoised SNR of 44.2 can be achieved using the improved threshold method. We further discuss the denoised results using different threshold functions, including the soft threshold function, hard threshold function, and improved threshold function. When using the wavelet base of sym6 and the improved threshold selection method, weak oscillations exist for the hard threshold function, and a similar but smoother RSCS shape can be obtained using the soft threshold and the improved threshold function. Moreover, the denoised SNR with the improved threshold function can reach 49.66, which is much higher than that for the soft and hard threshold of 46.22 and 44.15, respectively.

In addition, a large amount of water vapor Raman returned signals in the daytime measurements are involved in the de-noising discussion. It is demonstrated that an optimal daytime denoised evaluation can be achieved using the wavelet sym6, the improved threshold function, and the improved threshold selection.

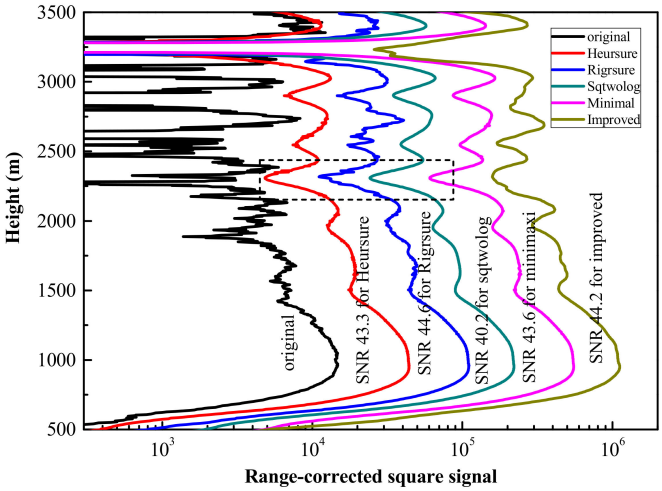

Figure 4. Comparison of denoised range-corrected square signals of daytime water vapor Raman scattering signal using different threshold selection methods.

3.3. Validation of the Daytime Performance

Furthermore, the daytime lidar performance can also be validated by a system SNR analysis. Figure 5 shows a measurement example taken at 16:00 CST on 15 September 2016, along with comparisons of the results before and after de-noising processing. Figure 5a shows the RSCS of water vapor and the nitrogen Raman scattering signal. Because of the solar background light, the effective detection range for water vapor was within a height of 2000 m. After de-noising processing, the noise was effectively removed from the water vapor Raman signal, and the effective detection distance was greatly improved to approximately 3200 m. The same denoised results can be obtained from the nitrogen Raman scattering signal. The retrieved water vapor mixing ratio is also compared in Figure 5b; the amount of water vapor is found to decrease with increasing height. In addition, the system SNR for water vapor measurement is discussed and compared. As shown in Figure 5c, the denoised system SNR for the daytime water vapor measurement was improved by approximately 3.4 times compared to that of the original signal. Under the condition of an SNR of 10, the effective detection range increases from 2000 m to 3200 m. Thus, the wavelet threshold de-noising method was verified to remove the background light and noise from the Raman scattering signals, and the daytime performance of Raman lidar could be improved effectively to provide data for the all-day variation in the water vapor.

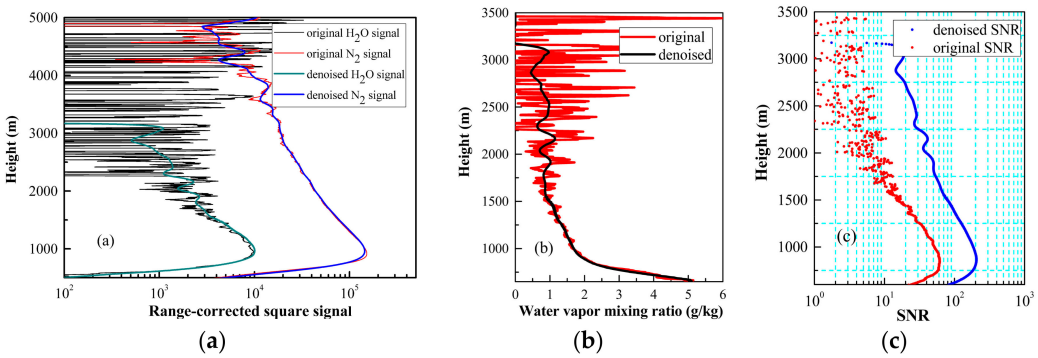

Figure 5. Comparison of the daytime lidar results before and after denoising. (**a**) range-corrected signal of water vapor and nitrogen Raman scattering; (**b**) water vapor mixing ratio profile; and (**c**) lidar signal to noise ratio (SNR) for the water vapor measurement.

4. Investigation of the All-Day Water Vapor Variation

It is known that atmospheric water vapor is characterized by rapid changes in time and space. To investigate the diurnal variation of water vapor, the all-day continuous observations were conducted using our Raman lidar, and the all-day atmospheric water vapor mixing ratio was obtained and analyzed, where the wavelet de-noising method was used to filter out the background noise in the daytime measurement. Moreover, a sunphotometer was used to retrieve the aerosol optical depth (AOD) at different wavelengths, and the total column water vapor content (TCWV) was also retrieved by the 940 nm absorption channel. The sunphotometer is only useful during cloudless daytime conditions, as it stops working when the sun is near sunset or during rainy weather. Therefore, the water vapor data collected by the sunphotometer were compared with the lidar data to validate the variation trend during the daytime.

4.1. Case Study 1

Figure 6 shows a measurement example of a 7-h THI plot of the water vapor mixing ratio taken during 15:00–22:00 CST on 15 September 2016. It is clearly shown that the atmospheric water vapor mixing ratio was larger during 15:00 and 17:00 in the afternoon and decreased slowly with time. An obvious change can be found in the water vapor distribution below 1.5 km. We also discuss the lidar PWV within two different layers: (1) ranging from the ground to 700 hPa and (2) ranging from

the ground to 850 hPa. The time series of lidar PWV is analyzed to investigate the diurnal variation trend in water vapor, as shown in Figure 7.

To clearly explain variations, the time series is divided into two periods: 15:00–18:00 and 18:00–22:00. The PWV below 700 hPa declined slowly from 16.5 mm to 15.5 mm during 15:00–17:00 and decreased rapidly to 14.5 mm in the next hour; a slight increase appeared after 18:00 and then leveled off with a value of 14 mm until 22:00 CST. The temporal change in PWV below 850 hPa is also shown in Figure 7. There was a modest PWV decrease before 17:00, with a sharp decline occurring at 17:00–18:00, and then, the trend was observed to be stable until 22:00 CST. Obviously, the variation trend in PWV below 700 hPa agrees well with that below 850 hPa. The PWV in both layers by lidar presented a downward trend from the afternoon to the night, with a larger PWV in the afternoon and a lower value in the evening.

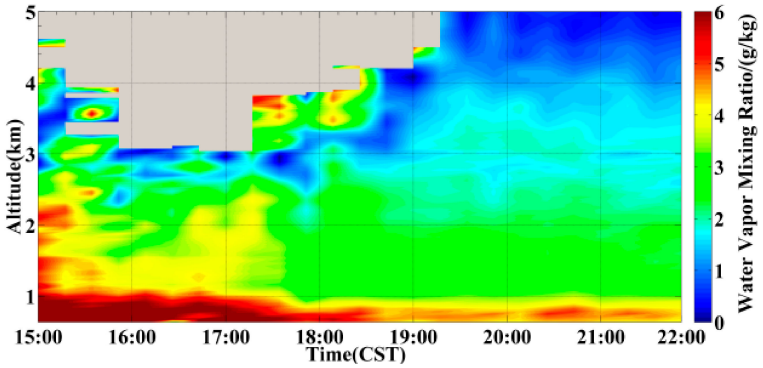

Figure 6. THI plot of water vapor mixing ratio during 15:00–22:00 CST on 15 September 2016, by Raman lidar.

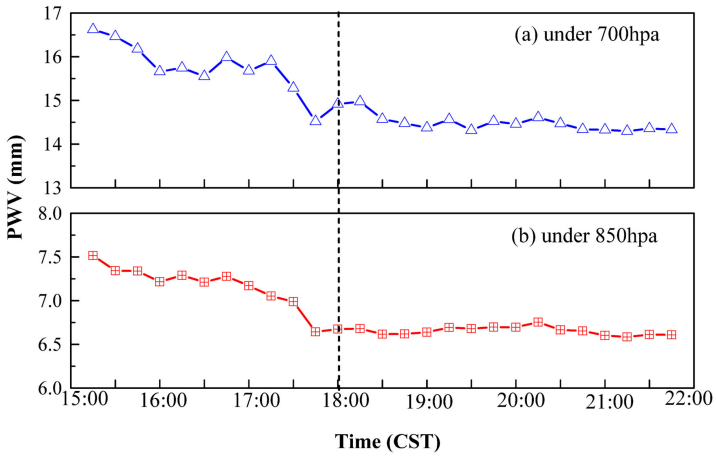

Figure 7. Variation trend in PWV in different layers by lidar at 15:00–22:00 CST on 15 September 2016.

To validate the variation trend during the daytime, the TCWV recorded by the sunphotometer was retrieved and compared with the PWV values of the corresponding time period. Figure 8 shows the time series of the AODs at different wavelengths and the TCWV during 15:00–17:48 CST. The data at other times are not available because of the sunset. It is clearly seen that the AODs gradually decrease with wavelength and that they all show a consistent trend of diurnal variation. The AOD values at 340 nm ranged from approximately 1.2 to 2.0 during the afternoon. The highest values of 2.0 occurred in the early afternoon, after which the AOD dropped to a value of 1.3 at 16:40 CST and then leveled off at 1.2 till 17:48 CST. The AOD values at a wavelength of 340 nm, 400 nm, 500 nm, 870 nm, and 1020 nm are used to determine the AOD value at 940 nm to obtain the TCWV. As shown

in Figure 8b, the TCWV values ranged from 20 mm to 35 mm, and the daily averaged content was approximately 25 mm. We can also see that the diurnal variation shows a stepwise trend, with a high value in the early afternoon and a low value in the late afternoon, in agreement with the variation trend in the PWV based on the Raman lidar measurements.

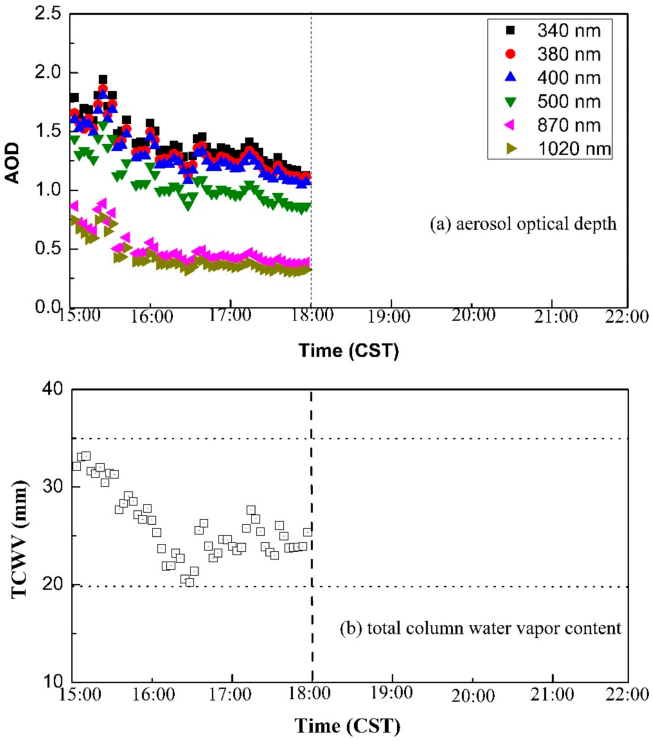

Figure 8. Time series of AODs at different wavelengths and column water vapor contents by sunphotometer during 15:00–18:00 on 15 September 2016.

The correlation analysis between TCWV and PWV at the two layers was also discussed, and the results are shown in Figure 9. We can see that TCWV and PWV at the layer below 700 hPa yield a good positive correlation with a correlation coefficient of 0.843, and a correlation coefficient of 0.81 was also obtained between TCWV and lidar PWV at the layer below 850 hPa. Therefore, it is indicated from this case study that the diurnal variation in atmospheric water vapor presents a downward trend across the entire afternoon, and also that the lidar PWV in the bottom layer has a good relationship with the total water vapor content.

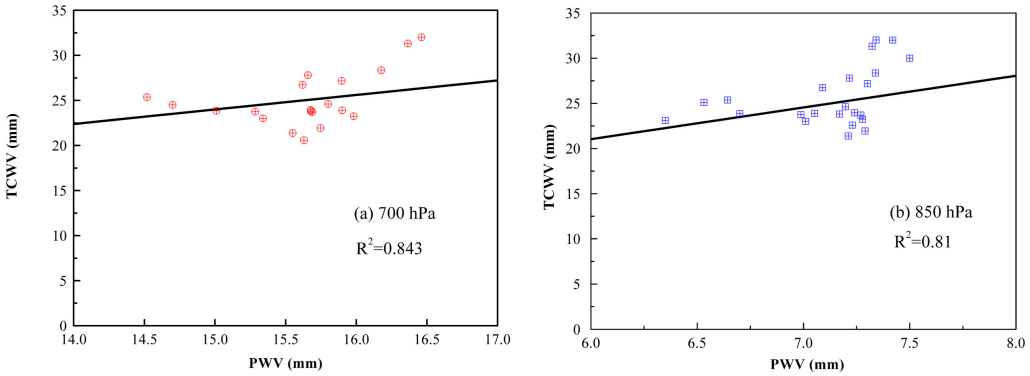

Figure 9. Correlation analysis of the total water vapor amount with PWV below 700 hPa and below 850 hPa.

4.2. Case Study 2

Another daytime measurement example was taken at 6:00–24:00 on 23 September 2016, under clear weather conditions. The temporal and height variation curve is clearly presented in the THI plot in Figure 10. Influenced by sun background light, a denoised water vapor measurement up to 3–4 km could be obtained from 8:00 to 16:00 in the daytime, and a detection range up to 6 km could be obtained for the rest of the time. Overall, the atmospheric water vapor mixing ratio is higher at the bottom and decreases gradually with the height. The water vapor mixing changed rapidly during the entire 18 h measurement; in particular, the water vapor mixing ratio at heights of 1–2.5 km showed an obviously rapid increase from 14:00 in the afternoon. Here, the time series divided the time into three periods, 6:00–12:00 during the morning, 12:00–18:00 during the afternoon, and 18:00–24:00 in the evening. To reveal the diurnal variation of water vapor during the daytime, the PWV time series below 700 hPa and 850 hPa are also shown in Figure 11. Taking the PWV below 850 hPa as an example, it declined slowly in the morning, reached a minimum value at 12:00, and then slowly increased in the afternoon before leveling off during the night. The consistent variation trend is also visible in the PWV below 700 hPa, despite the slight fluctuations.

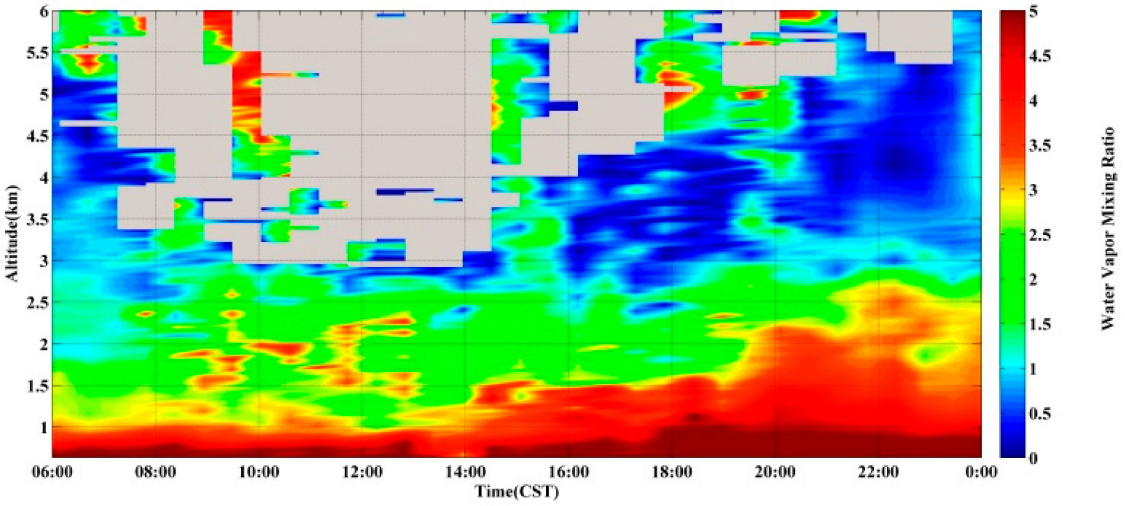

Figure 10. THI plot of water vapor mixing ratio from 6:00–24:00 on 22 September 2016.

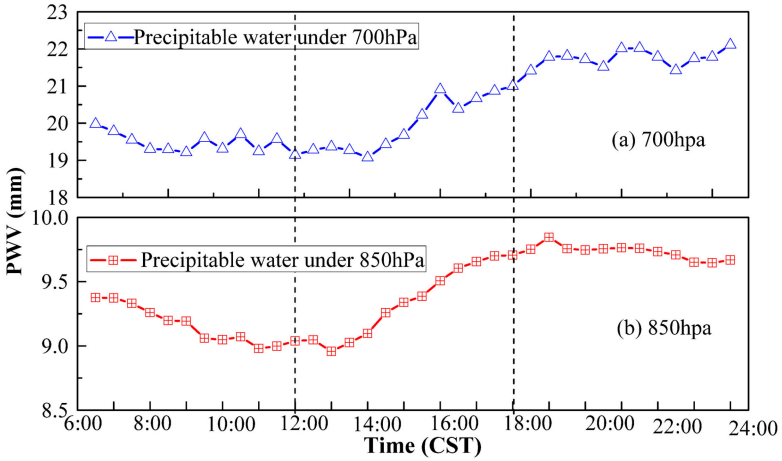

Figure 11. Variation trend in PWV in different layers by lidar at 6:00–24:00 CST on 22 September 2016.

We further analyzed the AODs and the TCWV results with the sunphotometer. As shown in Figure 12a, the AOD at individual wavelengths showed the same change tendency, where the AOD

was high in the morning and afternoon and low at noon. The AOD value of 1.0 at 340 nm occurred in the early morning, after which the AOD dropped off sharply to less than 0.80 by the mid-morning; it gradually increased through the afternoon, reaching a peak of 1.2 in the late afternoon. Moreover, the time series of TCWV was obtained and also shown in Figure 12. The water vapor content data from 6:00–18:00 collected by the sunphotometer are used to compare those obtained by the Raman lidar during the corresponding time period. A gentle diurnal variation trend can be observed in the atmospheric water vapor content, with the range from 13 mm to 30 mm during the daytime. The water vapor content was largerm with a value of ~30 mm in the early morning, and it decreased gradually in the morning until a valley appeared at noon, reaching a value of 13 mm. The water vapor content began to increase to ~31 mm through the afternoon. Thus, the overall characteristics presented a tendency of high in the morning and afternoon and low at noon. The lower water vapor content at approximately midday is mainly caused by the radiation of the sun. The trend of water vapor enhancement from the beginning of the afternoon is likely related to subsequent rainfall processes. A weak rainfall process occurred with precipitation of 0.4–2.4 mm during 23–24 September. Thus, the accumulation of water vapor indicates the potential preparation for precipitation. By comparison, we can find that the PWV in different layers measured by Raman lidar also has a consistent diurnal variation trend with the total amount of water vapor measured by the sunphotometer.

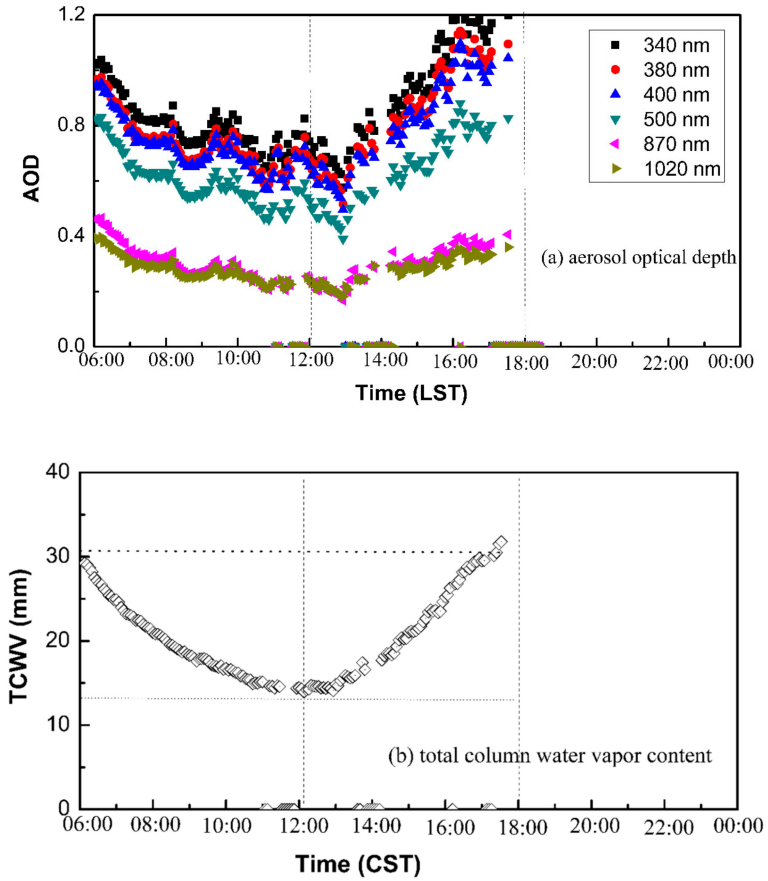

Figure 12. Time series of AODs at different wavelengths and column water vapor contents by sunphotometer at 6:00–18:00 on 22 September 2016.

By comparison, we can find that the PWV in different layers measured by Raman lidar also has a consistent diurnal variation trend with the total amount of water vapor measured by sunphotometer. Furthermore, we analyzed the correlation between TCWV and PWV below 850 hPa and 700 hPa, as shown in Figure 13; a good positive correlation was observed, with a correlation coefficient of >0.75

between the two sets of measurements. Thus, PWV in the different layers can accurately reveal the diurnal variation of atmospheric water vapor during the daytime and can be an indicator of the entire water vapor content.

The above continuous observations also reveal a different diurnal trend in water vapor, i.e., a downward trend from the afternoon to the night or a tendency of a high value in the morning and afternoon and a low value at noon. It is also inferred that the diurnal variation of the water vapor is complicated and has no obvious trend; this complicated response should be closely related to the weather conditions in the preceding and following period. In other words, the variation trend in the water vapor can in turn be an indicator of the weather to a certain extent.

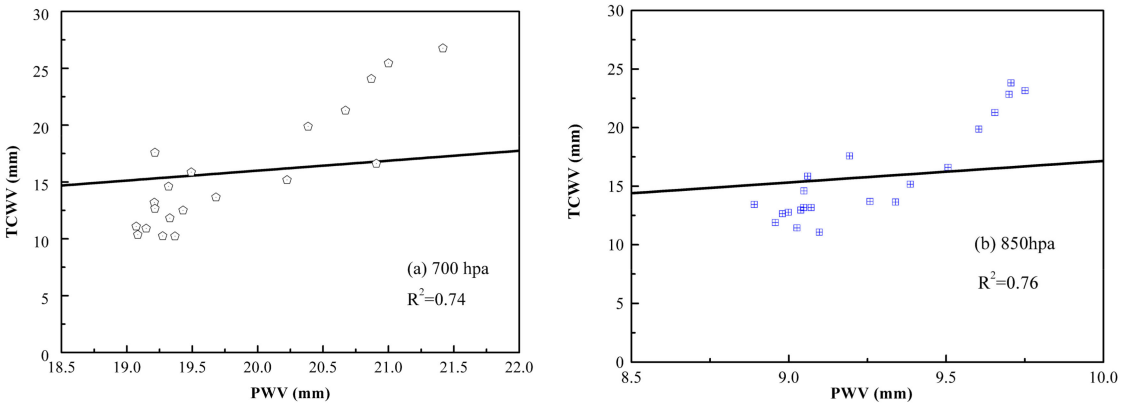

Figure 13. Correlation analysis of the total water vapor amount with PWV below 700 hPa and below 850 hPa.

5. Summary

Raman lidar and sunphotometer measurements are combined to investigate the all-day variation characteristics in the water vapor distribution in Xi'an, China (34.233°N, 108.911°E).

The daytime performance of the Raman lidar system for measuring water vapor profiles was first discussed. The wavelet threshold denoising method was used to filter out the strong solar background light in daytime. Via the denoising process and evaluations, it was demonstrated that the best denoising effect could be achieved by following the optimized conditions: wavelet sym6, improved threshold function, and improved threshold selection. The daytime performance for the Raman lidar water vapor measurement SNR was found to be improved by ~3.4 times up to a height of 3 km compared to that of the original signal.

Furthermore, comparisons of PWV in different layers by lidar and the total column water vapor content recorded by the sunphotometer were combined to study the daytime temporal and spatial variations of water vapor. Through two case studies, the PWV values within the layers below 700 hPa and 850 hPa as measured by lidar were found to have a consistent diurnal variation trend with the TCWV measured by the sunphotometer; a good positive correlation with a correlation coefficient of >0.75 between them was obtained, indicating that the atmospheric content in the bottom layer measured by lidar can accurately reveal the diurnal variation of atmospheric water vapor during the daytime, and can be an indicator of the entire water vapor content.

In addition, despite only two examples being considered in this paper, different diurnal trends in the water vapor were revealed: a downward trend from the afternoon to the night or a tendency to have a high value in the morning and afternoon and a low value at noon. It is also inferred that the diurnal variation of the precipitable water vapor is complicated and lacks a definite trend; this complicated behavior should be closely related to the weather conditions in the preceding and following periods, and the variation trend in the water vapor can in turn be an indicator of the weather to a certain extent.

Author Contributions: Conceptualization, Y.W., L.T., T.G. and D.H. Methodology, Y.W., L.T. and D.H. Resources, Y.W., L.T., T.G., Q.W and C.L. Original draft preparation, Y.W. and L.T. Writing, Y.W. and L.T. Review and editing, Y.W., Y.S. and D.H. Visualization, L.T., T.G., C.L. Supervision, Y.W. and D.H. Project administration, Y.W. and D.H. Funding acquisition, Y.W. and D.H.

Funding: This work was supported by the National Natural Science Foundation of China (NSFC) (grant Nos. U1733202, 41627807, 41575027, 61308105 and 41027004).

Conflicts of Interest: The authors declare no conflicts of interest.

References

1. Wang, C.X.; Gao, S.T.; Liang, L.; Deng, D.F.; Gong, H.N. Multi-scale characteristics of moisture transport during a rainstorm process in North China. *Atmos. Res.* **2014**, *145*, 189–204. [CrossRef]
2. Ye, H.; Fetzer, E.J.; Wong, S.; Behrangi, A.; Yang, D.; Lambrigtson, B.H. Increasing atmospheric water vapor and higher daily precipitation intensity over northern Eurasia. *Geophys. Res. Lett.* **2016**, *42*, 9404–9410. [CrossRef]
3. Raval, A.; Ramanathan, V. Observational determination of the greenhouse effect. *Nature* **1989**, *342*, 758–761. [CrossRef]
4. Held, I.M.; Soden, B.J. Robust responses of the hydrological cycle to global warming. *J. Clim.* **2010**, *19*, 5686–5699. [CrossRef]
5. Solomon, S.; Rosenlof, K.H.; Portmann, R.W.; Daniel, J.S.; Davis, S.M.; Sanford, T.J.; Plattner, G.-K. Contributions of stratospheric water vapor to decadal changes in the rate of global warming. *Science* **2010**, *327*, 1219–1223. [CrossRef] [PubMed]
6. Tregoning, P.; Boers, R.; O'Brien, D.; Hendy, M. Accuracy of absolute precipitable water vapor estimates from GPS observations. *J. Geophys. Res. Atmos.* **1998**, *103*, 28701–28710. [CrossRef]
7. Fetzer, E.J.; Lambrigtsen, B.H.; Eldering, A.; Aumann, H.H.; Chahine, M.T. Biases in total precipitable water vapor climatologies from atmospheric infrared sounder and advanced microwave scanning radiometer. *J. Geophys. Res. Atmos.* **2006**. [CrossRef]
8. Mattis, I.; Ansmann, A.; Althausen, D.; Jaenisch, V.; Wandinger, U.; Müller, D.; Arshinov, Y.F.; Bobrovnikov, S.M.; Serikov, I.B. Relative-humidity profiling in the troposphere with a Raman lidar. *Appl. Opt.* **2002**, *41*, 6451–6462. [CrossRef] [PubMed]
9. Pandolfi, M.; Amodeo, A.; Mona, L.; Pappalardo, G. Lidar measurements of atmospheric aerosol, water vapour and clouds. *Recent Res. Dev. Opt.* **2003**, *3*, 543–562.
10. De Tomasi, F.; Perrone, M.R. Lidar measurements of tropospheric water vapour and aerosol profiles over south-eastern Italy. *J. Geophys. Res.* **2003**, *108*, 9–12. [CrossRef]
11. Navas-Guzmán, F.; Fernández-Gálvez, J.; Granados-Muñoz, M.J.; Guerrero-Rascado, J.L.; Bravo-Aranda, J.A.; Alados-Arboledas, L. Tropospheric water vapour and relative humidity profiles from lidar and microwave radiometry. *Atmos. Meas. Tech.* **2014**, *7*, 1201–1211. [CrossRef]
12. Jia, J.; Yi, F. Atmospheric temperature measurements at altitudes of 5–30 km with double-grating-based pure rotational Raman lidar. *Appl. Opt.* **2014**, *53*, 5330–5343. [CrossRef] [PubMed]
13. Behrendt, A.; Nakamura, T.; Onishi, M.; Baumgrat, R.; Tsuda, T. Combined Raman lidar for the measurement of atmospheric temperature, water vapor, particle extinction coefficient, and particle backscatter coefficient. *Appl. Opt.* **2002**, *41*, 7657–7666. [CrossRef] [PubMed]
14. Wang, Y.; Fu, Q.; Zhao, M.; Gao, F.; Di, H.; Song, Y.; Hua, D. A UV multifunctional Raman lidar system for the observation and analysis of atmospheric temperature, humidity, aerosols and their conveying characteristics over Xi'an. *J. Quant. Spectrosc. Radiat. Transf.* **2018**, *205*, 114–126.
15. Whiteman, D.N. Examination of the traditional Raman lidar technique. II. Evaluating the ratios for water vapor and aerosol. *Appl. Opt.* **2003**, *42*, 2593–2608. [CrossRef] [PubMed]
16. Xie, C.; Zhou, J.; Yue, G.-M.; Fan, A.-Y. Mobile lidar system for measuring tropospheric aerosol and water vapor. *Infrared Laser Eng.* **2007**, *36*, 365–367.
17. Bedoya-Velásquez, A.E.; Navas-Guzmán, F.; Granados-Muñoz, M.J.; Titos, G.; Román, R.; Andrés Casquero-Vera, J.; Ortiz-Amezcua, P.; Antonio Benavent-Oltra, J.; De Arruda Moreira, G.; Montilla-Rosero, E.; et al. Hygroscopic growth study in the framework of EARLINET during the SLOPE i campaign: Synergy of remote sensing and in situ instrumentation. *Atmos. Chem. Phys.* **2018**, *18*, 7001–7017. [CrossRef]

18. Granados-Muñoz, M.J.; Navas-Guzmán, F.; Bravo-Aranda, J.A.; Guerrero-Rascado, J.L.; Lyamani, H.; Valenzuela, A.; Titos, G.; Fernández-Gálvez, J.; Alados-Arboledas, L. Hygroscopic growth of atmospheric aerosol particles based on active remote sensing and radiosounding measurements: Selected cases in southeastern Spain. *Atmos. Meas. Tech.* **2015**, *8*, 705–718. [CrossRef]
19. Tsekeri, A.; Amiridis, V.; Marenco, F.; Nenes, A.; Marinou, E.; Solomos, S.; Rosenberg, P.; Trembath, J.; Nott, G.J.; Allan, J.; et al. Profiling aerosol optical, microphysical and hygroscopic properties in ambient conditions by combining in situ and remote sensing. *Atmos. Meas. Tech.* **2017**, *10*, 83–107. [CrossRef]
20. Veselovskii, I.; Whiteman, D.N.; Kolgotin, A.; Andrews, E.; Korenskii, M. Demonstration of aerosol property profiling by multiwavelength lidar under varying relative humidity conditions. *J. Atmos. Ocean. Tech.* **2009**, *26*, 1543–1557. [CrossRef]
21. Guerrero-Rascado, J.; Ruiz, B.; Chourdakis, G.; Georgoussis, G.; Alados-Arboledas, L. One year of water vapour Raman lidar measurements at the Andalusian Centre for Environmental Studies (CEAMA). *Int. J. Remote Sens.* **2008**, *29*, 5437–5453. [CrossRef]
22. Froidevaux, M.; Higgins, C.W.; Simeonov, V.; Ristori, P.; Pardyjak, E.; Serikov, I.; Calhoun, R.; den Bergh, H.V.; Parlange, M.B. A Raman lidar to measure water vapor in the atmospheric boundary layer. *Adv. Water Res.* **2013**, *51*, 345–356. [CrossRef]
23. Leblanc, T.; McDermid, I.S.; Walsh, T.D. Ground-based water vapor Raman lidar measurements up to the upper troposphere and lower stratosphere for long-term monitoring. *Atmos. Meas. Tech.* **2012**, *5*, 17–36. [CrossRef]
24. Wang, Y.; Cao, X.; He, T.; Gao, F.; Hua, D.; Zhao, M. Observation and analysis of the temperature inversion layer by Raman lidar up to the lower stratosphere. *Appl. Opt.* **2015**, *54*, 10079–10088. [CrossRef] [PubMed]
25. Mazzola, M.; Stone, R.S.; Herber, A.; Tomasi, C.; Lupi, A.; Vitale, V.; Lanconelli, C.; Toledano, C.; Cachorro, V.E.; O'Neill, N.T.; et al. Evaluation of sun photometer capabilities for retrievals of aerosol optical depth at high latitudes: The POLAR-AOD intercomparison campaigns. *Atmos. Environ.* **2012**, *52*, 4–17. [CrossRef]
26. Toledano, C.; Cachorro, V.E.; Gausa, M.; Stebel, K.; Aaltonen, V.; Berjón, A.; de Galisteo, J.P.O.; de Frutos, A.M.; Bennouna, Y.; Blindheim, S.; et al. Overview of sun photometer measurements of aerosol properties in Scandinavia and Svalbard. *Atmos. Environ.* **2012**, *52*, 18–28. [CrossRef]
27. Dubovik, O.; Holben, B.; Eck, T.F.; Smirnov, A.; Kaufman, Y.J.; King, M.D.; Tanré, D.; Slutsker, I. Variability of absorption and optical properties of key aerosol types observed in worldwide locations. *J. Atmos. Sci.* **2002**, *59*, 590–608. [CrossRef]
28. Hu, X.; Liu, J.; Sun, L.; Rong, Z.; Li, Y.; Zhang, Y.; Zheng, Z.; Wu, R.; Zhang, L.; Gu, X. Characterization of CRCS Dunhuang test site and vicarious calibration utilization for Fengyun (FY) series sensors. *Can. J. Remote Sens.* **2010**, *36*, 566–582. [CrossRef]
29. Schmid, B.; Wehrli, C. Comparison of Sun photometer calibration by use of the Langley technique and the standard lamp. *Appl. Opt.* **1995**, *34*, 4500–4512. [CrossRef] [PubMed]
30. Michalsky, J.J.; Liljegren, J.C.; Harrison, L.C. A comparison of sun photometer derivations of total column water vapor and ozone to standard measures of same at the southern great plains atmospheric radiation measurement site. *J. Geophys. Res. Atmos.* **1995**, *100*, 25995–26003. [CrossRef]
31. Halthore, R.N.; Eck, T.F.; Holben, B.N.; Markham, B.L. Sun photometric measurements of atmospheric water vapor. *J. Geophys. Res. Atmos.* **1997**, *102*, 4243–4352. [CrossRef]
32. Ichoku, C.; Levy, R.; Kaufman, Y.J.; Remer, L.A.; Li, R.-R.; Martins, V.-J.; Holben, B.N.; Abuhassan, N.; Slutsker, I.; Eck, T.F. Analysis of the performance characteristics of the five-channel Microtops II Sun photometer for measuring aerosol optical thickness and precipitable water vapor. *J. Geophys. Res.* **2002**, *107*. [CrossRef]
33. Wu, S.H.; Liu, Z.S.; Liu, B.Y. Enhancement of lidar back scatters signal to noise ratio using empirical mode decomposition method. *Opt. Commun.* **2006**, *267*, 137–144. [CrossRef]
34. Tian, P.; Cao, X.; Liang, J.; Zhang, L. Improved empirical mode decomposition based denoising method for lidar signals. *Opt. Commun.* **2014**, *325*, 54–59. [CrossRef]
35. Zhou, Z.; Hua, D.; Wang, Y.; Yan, Q.; Li, S.; Li, Y.; Wang, H. Improvement of the signal to noise ratio of Lidar echo signal based on wavelet de-noising technique. *Opt. Lasers Eng.* **2013**, *51*, 961–966. [CrossRef]
36. Mix, D.F.; Olejniczak, K.J. Elements of wavelets for engineers and scientists. *Phys. Today* **2005**, *58*, 54.

37. Thakur, K.V.; Ambhore, P.G.; Sapkal, A.M. Novel technique for performance improvement of the wavelet based denoising algorithms using rotated wavelet filters. *Procedia Comput. Sci.* **2016**, *79*, 499–508. [CrossRef]
38. Mallat, S.; Hwang, M.L. Singularity detection and processing with wavelet. *IEEE Trans. IT* **1992**, *38*, 617–643. [CrossRef]
39. Tzabazis, A.; Eisenried, A.; Yeomans, D.C.; Hyatt, M., IV. Wavelet analysis of heart rate variability: Impact of wavelet selection. *Biomed. Signal Process. Control* **2018**, *40*, 220–225. [CrossRef]
40. Genovese, L.; Neelov, A.; Goedecker, S.; Deutsch, T.; Ghasemi, S.A.; Willand, A.; Caliste, D.; Zilberberg, O.; Rayson, M.; Bergman, A.; et al. Daubechies wavelets as a basis set for density functional pseudopotential calculations. *J. Chem. Phys.* **2008**, *129*. [CrossRef] [PubMed]
41. Abdolmaleki, M.; Tabaei, M.; Fathianpour, N.; Gorte, B.G.H. Selecting optimum base wavelet for extracting spectral alteration features associated with porphyry copper mineralization using hyperspectral images. *Int. J. Appl. Earth Obs. Geoinform.* **2017**, *58*, 134–144. [CrossRef]
42. Luo, W.; Chen, F. Improved wavelet-denoising method. *Infrared Laser Eng.* **2008**, *37*, 226–228.
43. Krim, H.; Tucker, D.; Mallat, S.; Donoho, D. On denoising and best signal representation. *IEEE Trans. Inf. Theory* **1997**, *45*, 2225–2238. [CrossRef]
44. Donoho, D.L.; Johnstone, I.M. Threshold selection for wavelet shrinkage of noisy data. In Proceedings of the 16th Annual International Conference of the IEEE Engineering in Medicine and Biology Society, Baltimore, MD, USA, 3–6 November 1994.
45. Cui, H.; Zhao, R.; Hou, Y. Improved threshold denoising method based on wavelet transform. *Phys. Procedia* **2012**, *33*, 1354–1359.

© 2018 by the authors. Licensee MDPI, Basel, Switzerland. This article is an open access article distributed under the terms and conditions of the Creative Commons Attribution (CC BY) license (http://creativecommons.org/licenses/by/4.0/).